Philosophical Magazine
Publication details, including instructions for authors and subscription information:
http://www.tandfonline.com/loi/tphm20

Atomistic study of temperature and strain rate-dependent phase transformation behaviour of NiTi shape memory alloy under uniaxial compression

Qiuyun Yin[a], Xianqian Wu[a], Chenguang Huang[a], Xi Wang[b] & Yanpeng Wei[a]

[a] Key Laboratory of Mechanics in Fluid Solid Coupling Systems, Institute of Mechanics, Chinese Academy of Sciences, Beijing 100190, People's Republic of China

[b] School of Mechanical, Electronic and Control Engineering, Beijing Jiaotong University, Beijing 100044, People's Republic of China

Published online: 16 Jul 2015.

To cite this article: Qiuyun Yin, Xianqian Wu, Chenguang Huang, Xi Wang & Yanpeng Wei (2015): Atomistic study of temperature and strain rate-dependent phase transformation behaviour of NiTi shape memory alloy under uniaxial compression, Philosophical Magazine, DOI: 10.1080/14786435.2015.1065018

To link to this article: http://dx.doi.org/10.1080/14786435.2015.1065018

Philosophical Magazine, 2015
http://dx.doi.org/10.1080/14786435.2015.1065018

Taylor & Francis
Taylor & Francis Group

Atomistic study of temperature and strain rate-dependent phase transformation behaviour of NiTi shape memory alloy under uniaxial compression

Qiuyun Yin[a], Xianqian Wu[a]*, Chenguang Huang[a], Xi Wang[b] and Yanpeng Wei[a]

[a]*Key Laboratory of Mechanics in Fluid Solid Coupling Systems, Institute of Mechanics, Chinese Academy of Sciences, Beijing 100190, People's Republic of China;* [b]*School of Mechanical, Electronic and Control Engineering, Beijing Jiaotong University, Beijing 100044, People's Republic of China*

(*Received 2 April 2015; accepted 18 June 2015*)

Molecular dynamics simulation was conducted to investigate the phase transformation behaviour of nickel–titanium (NiTi, 50%-50% at.%) nanopillar under uniaxial compression at loading rates varying from 3.30×10^7 to 3.30×10^9 s^{-1} and at temperatures varying from 325 to 600 K. The phase transformation of NiTi was observed to be sensitive to loading rates and temperatures. The phase transformation stress of B2 → B19 increased with increasing temperature while it was insensitive to loading rate. The phase transformation stress of B19 → B19′ → BCO increased with increasing strain rate and decreasing temperature. In addition, reverse phase transformation was observed during compression due to the interaction between the phase transformation of B19 → B19′ → BCO and the deformation twinning/dislocation slide-induced plasticity of the BCO phase, leading to different residual crystal structures after loading. Moreover, a diagram for the phase transformation behaviour of NiTi in the simulated ranges of strain rate and temperature was obtained, from which the contrary experimental observations on the phase transformation behaviour of NiTi from the studies of Nemat-Nasser et al. (Mech. Mater. 37 (2005) p.287) and Liao et al. (J. Appl. Phys. 112 (2012) p.033515) at various strain rates could be well explained.

Keywords: molecular dynamics; phase transformation behaviour of NiTi; strain rate effect; temperature effect; reverse phase transformation

1. Introduction

Shape memory alloys (SMAs) are a class of metal alloys that show unique property of shape memory effect, i.e. deformation at low temperature can be recovered with aid of heating [1,2]. Generally, the shape memory effect is regarded to be a result of transformation and reverse transformation between the initial austenite and the deformed martensite phases [3–5]. SMAs can also exhibit pseudo-elasticity (or super-elasticity, SE) with a recoverable strain up to 8% during loading with the similar phase transformation mechanism as the shape memory effect [1]. Due to these unique

*Corresponding author. Email: wuxianqian@imech.ac.cn

properties, SMAs have found applications in variety of fields including aeronautics [2], biomedicine [6,7], to name a few.

Nickel–titanium (NiTi) alloy is a typical SMA. It exhibits SE while the test temperature is close to the austenite finish temperature (A_f) [8–14]. A considerable body of experiments has been conducted on NiTi alloys to investigate its strain rate and temperature-dependent phase transformation behaviour [11,12,14–19]. Nemat-Nasser et al. [8,9] studied the dynamic behaviour of NiTi at various strain rates in a range of 10^{-3} to about 2×10^4 s^{-1} and at temperatures in a range of 77–400 K. The results showed that the SE behaviour of NiTi was more sensitive to temperature than to strain rate. A critical temperature and a certain strain rate (less than 17,000 s^{-1}) for the martensitic transformation were observed. Nevertheless, Liao et al. [10] investigated the phase transformation of NiTi at high strain rates in a range of 10^5–10^7 s^{-1} implemented by laser shock processing. Martensites were observed in the shocked regions of the NiTi specimens after experiments. In addition, our recent research from laser shock experiments showed that the martensitic transformation of NiTi was controlled by both loading rates and applied peak pressures, and a critical shock pressure was required for the martensitic transformation of NiTi at ultrahigh strain rates up to 10^7 s^{-1}. It could be found that the strain rate and the temperature effects on phase transformation behaviour of NiTi show controversy in the aforementioned researches. Further studies are needed to clearly interpret the strain rate and temperature-dependent phase transformation behaviour of NiTi.

Molecular dynamics (MD) simulation, which can capture the details at the atomic level and reveal the intrinsic mechanisms of macroscopic properties of materials, provides an atomic insight into the phase transformation mechanism of NiTi. A large body of researches has studied the mechanisms of SE and SME of NiTi by MD simulations. The study by Wu et al. [20] showed that dislocation nucleation started from surfaces during torsional deformation of NiTi nanowires. The study by Zhong et al. [13,21] showed that complex phase transformation behaviour including the super-elasticity and the shape memory effects of NiTi nanostructures was observed during compressive loading and unloading. Tomohiro et al. [22] studied the microscopic mechanism of stress-induced martensitic transformation of NiTi alloys. The results showed that there were multiple pathways between the parent phase and the martensite phase regardless of strain rate. The studies by Wu et al. [20], Zhong et al. [13,21] and Tomohiro et al. [22] revealed some of phase transformation mechanisms of NiTi alloys including the phase transformation pathway and the variants of different phases of NiTi as well as the effects on the phase transformation behaviour. These results provided a better understanding of the pseudo-elasticity and the shape memory behaviour of NiTi alloys. However, atomistic characterization of phase transformation of NiTi are required to better understand the strain rate and temperature-dependent phase transformation behaviour of NiTi alloys, so that the controversial observations from the studies of Nemat-Nasser et al. [8] and Liao et al. [10] at various strain rates and temperatures could be well explained.

In the present research, the strain rate and temperature-dependent phase transformation behaviour of a monocrystalline NiTi nanopillar under uniaxial compression was studied by MD simulation. The computational model was built using the same method as Zhong et al. [13]. The stress versus strain curves, the common neighbour analysis (CNA) [23] and the atomic structure evolution were undertaken to illustrate the phase transformation behaviour of the NiTi nanopillar at various strain rates and temperatures. The paper was organized as follows. The potential function for describing the

interaction between atoms of NiTi, the atomic structures and the computational models were illustrated in Section 2. The simulated results of the NiTi nanopillar at various strain rates and temperatures were given in Section 3. In Section 4, summary of computational results and discussion were presented.

2. Method

2.1. *Potential*

Embedded atom method (EAM) potential, which is regarded as the most efficient potential for metals, is taken to describe the interatomic interactions of NiTi. Several EAM potentials were developed to describe the various properties of NiTi. In the present research, an EAM potential for NiTi, which was originally developed by Lai and Liu [24] and improved by Zhong et al. [13], was taken to investigate the strain rate and temperature-dependent phase transformation behaviour of NiTi. The potential with a modified atomic force treatment near the cut off zone is expressed as

$$E = \sum_i \left\{ \sum_{i \neq j} A_{\alpha\beta} \exp\left[-p_{\alpha\beta} \left(\frac{r_{ij}}{d_{\alpha\beta}} - 1 \right) \right] - \sqrt{\sum_{i \neq j} F\left(r_{ij}\right)} \right\}, \tag{1}$$

where

$$F\left(r_{ij}\right) = \begin{cases} \xi_{\alpha\beta}^2 \exp\left[-2q_{\alpha\beta} \left(\frac{r_{ij}}{d_{\alpha\beta}} - 1 \right) \right], & r_{ij} < r_1 \\ c_{3,\alpha\beta}\left(r_{ij} - r_1\right)^3 + c_{2,\alpha\beta}\left(r_{ij} - r_1\right)^2 + c_{1,\alpha\beta}\left(r_{ij} - r_1\right) + c_{0,\alpha\beta}, & r_1 < r_{ij} < r_c \end{cases} \tag{2}$$

Here E is the total potential of all atoms, F describes the effects of electronic cloud density, d denotes the equilibrium distance of two atoms, r_{ij} is the distance between atom i and j and α and β represent the types of atoms, i.e. atom Ni and atom Ti, respectively. In addition, A, p, ξ and q are determined by the *ab initio* calculation result, and $c_{0,\alpha\beta}$, $c_{1,\alpha\beta}$, $c_{2,\alpha\beta}$ and $c_{3,\alpha\beta}$ are the fitting parameters decided by r_1. The first term of Equation (1) is the pair interaction of two atoms, and the second term describes the many-body effect. The potential related parameters for NiTi are given in Table 1. The cutoff radius r_c was set to be 4.2 Å and r_1 to be 4.0 Å [21]. According to the previous studies [24], the potential could well predict NiTi's properties such as lattice constant. In the present simulation, the system was fully relaxed by using stress-controlled conjugate gradient energy minimization.

Table 1. Potential parameters for NiTi.

Parameters	Ni–Ni	Ti–Ti	Ni–Ti
d (Å)	2.490	2.950	2.607
A (eV)	0.104	0.153	0.300
p	11.198	9.253	7.900
ξ (eV)	1.591	1.879	2.480
Q	2.413	2.513	3.002
c_3	27.3341	122.395	47.8513
c_2	−7.54308	−34.205	−12.92362
c_1	−0.26286	−1.0054	−0.572708
c_0	0.13561	0.59012	0.248676

2.2. *MD modelling*

The large-scale atom/molecular massively parallel simulation (LAMMPS) [25], which is a widely used open source software, is undertaken to simulate the phase transformation behaviour of an NiTi nanopillar under uniaxial compression at various strain rates and temperatures. As shown in Figure 1(a), the initial microstructure of the NiTi nanopillar was set to be B2 phase, which was an austenite phase with the microstructure same as CsCl. A nanopillar with a length of 24.9 nm and a cross section of 4.9 nm × 5.2 nm, which consisted of 46,080 atoms, was constructed. The $\langle 1\,1\,0 \rangle$ direction, denoted by axis *y*, was set to be the loading direction. The periodic boundary condition was applied in the loading direction while the sidewalls of the nanopillar were set to be traction-free. The time increment of simulation was 0.5 fs. Different initial simulation models

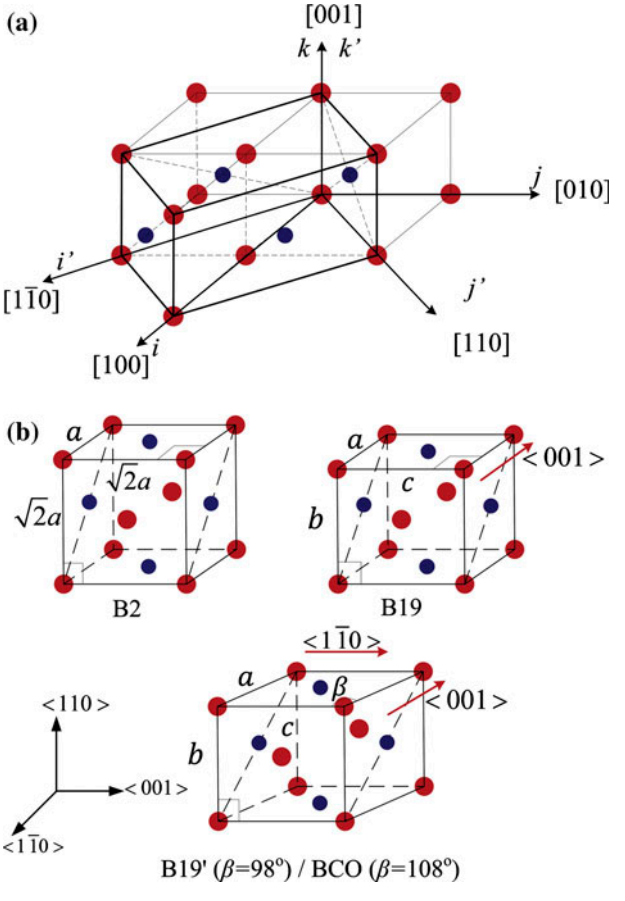

Figure 1. (colour online) (a) Schematic of a NiTi unit cell with a phase of B2. Letters *i*, *j* and *k* denoted the crystal directions of [1 0 0] , [0 1 0] and [0 0 1], respectively. The coordinate directions *x*, *y*, *z* used in the present study were assigned along *i*′, *j*′, *k*′ with the directions of [1 $\bar{1}$ 0], [1 1 0] and [0 0 1], respectively. (b) Schematic of NiTi units cell with phases of B2, B19, B19′ and BCO, respectively.

through thermal relaxing at temperatures varying from 325 (between the martensite start temperature M_s ~310 K and the austenite start temperature A_s ~350 K [21]) to 600 K were built to investigate the temperature effects on the phase transformation behaviour of the NiTi nanopillar. During the thermal relaxing, the nanopillar was fully relaxed at zero pressure for 100 ps, achieved by 200,000 MD time steps.

After the thermal relaxing, the strain-controlled uniaxial compression was applied on the NiTi nanopillar along the loading direction, i.e. various imposed displacements in the loading direction of the atoms were applied at every loading step (2,000 simulation time increments) according to the applied strain rates and atoms' positions. Various loading rates varying from 3.30×10^7 to 3.30×10^9 s^{-1} were simulated to investigate the strain rate-dependent phase transformation behaviour. Note that the compressive engineering strains were undertaken during loading. In the simulation, the phases of the NiTi were distinguished by the lattice parameters, the internal atomic shuffling and the monoclinic angle β ($\beta = 90°$ for B2 and B19, $\beta = 98°$ for B19′ and $\beta = 108°$ for BCO [13]) as shown in Figure 1(b).

The simulation procedure was as follows. Firstly, the phase transformation behaviour as well as the stress versus strain curve of the NiTi nanopillar at a loading strain up to 10.23%, which was implemented by 620,000 time steps at a constant strain rate of 3.30×10^8 s^{-1} followed by an unloading to zero strain with the same time steps, was simulated and compared with the results of Zhong et al. [13] to validate the MD model. Secondly, the temperature effects on the phase transformation and the plastic deformation of the NiTi nanopillar at a constant strain rate of 8.25×10^8 s^{-1} were simulated at various temperatures varying from 325 to 600 K. Then, the phase transformation and the plastic deformation behaviour of the NiTi nanopillar at various strain rates in a range of 3.30×10^7–3.30×10^9 s^{-1} and at a temperature of 400 K were simulated to investigate the strain rate effects. Finally, the temperature and strain rate-dependent phase transformation behaviour of NiTi was analysed and discussed based on the simulation results.

3. Results and discussion

3.1. *MD model validation*

Firstly, the phase transformation behaviour of the NiTi nanopillar at a loading strain up to 10.23% and at a constant strain rate of 3.30×10^8 s^{-1} was simulated. The simulated stress versus strain curve is depicted in Figure 2(a). The NiTi nanopillar was observed to experience elastic deformation and then the complex phase transformation process of B2 → B19 → B19′ → BCO at various strains and ultimately slip-induced plasticity of BCO. In addition, the second-order displacement phase transition [26] during B2 → B19 was observed. Two types of atom shuffling modes, $\{1\,1\,0\}\langle 0\,0\,1\rangle$ shuffling that has a lowest energy barrier of NiTi [27] and $\{1\,1\,0\}\langle 1\,\bar{1}\,1\rangle$ shuffling that has the second lowest energy barrier [28], were also observed as shown in Figure 2(b). It could be seen that the present MD simulation captured the complex phase transformation behaviour of the NiTi nanopillar as the same as the study of Zhong et al. [13].

3.2. *Temperature effects*

In this section, the MD simulation at various temperatures varying from 325 to 600 K and at a constant strain rate of 8.25×10^8 s^{-1} was performed to investigate the

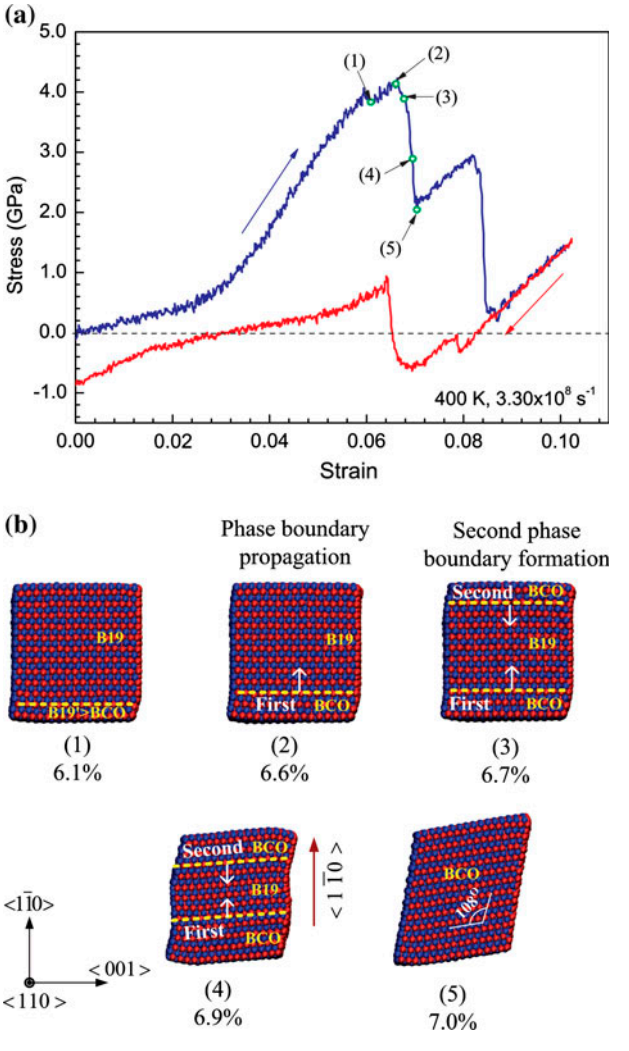

Figure 2. (colour online) Compression of the NiTi nanopillar at 400 K and at a constant strain rate of 3.3×10^8 s^{-1}. (a) Stress versus strain curve. (b) Cross-sectional view of the nanopillar, showing the atom shuffling direction.

temperature effects on the phase transformation of the NiTi nanopillar. The CNA was used to distinguish various phases during phase transformation. The CNA is a useful method for determining the local crystal structures around atoms. It can distinguish five crystal lattice with specific values in LAMMPS [25], i.e. 1 for FCC, 2 for HCP, 3 for BCC, 4 for icosahedral and 5 for the rest structures representing the B19′ or the BCO in the present study. Here, the phase transformation behaviour of the NiTi nanopillar was studied according to the change of its average CNA value. Note that CNA cannot distinguish the phases of B2 and B19 due to the slight difference in lattice parameters. Figure 3(a) shows the stress versus strain curve and the corresponding average CNA at

a temperature of 325 K and at a strain rate of 8.25×10^8 s^{-1}. As shown in Figure 3(a), at a temperature of 325 K that was close to the martensite start temperature and austenite start temperature, the stress increased non-linearly with increasing strain in a small strain range, indicating the initial metastable B2 phase of NiTi developed quickly to the relative stable B19 phase under applied compressive loading. The corresponding CNA value stayed at about 3.4, which was a little higher than the ideal CNA value of 3 for BCC due to the imperfect unit cell on surfaces. Then, the nanopillar with the newly formed B19 phase deformed elastically and the corresponding CNA was almost constant until the applied strain reached about 3.5%. A sudden decrease of stress and a corresponding dramatic increase of CNA were observed at a strain of 3.5%, indicating the formation of B19′ phase with a CNA value of 5 that caused by the shuffling of atoms in the $\langle 0\,0\,1 \rangle$ direction of the surface atoms on the $\{1\,1\,0\}$ plane as shown in Figure 3(b). The newly formed B19′ phase completely transformed to the BCO phase at a strain of 3.8% because of the influence of free surfaces. Then, the stress increased linearly to the peak value of 5.4 GPa at a strain of 4.3% while the newly formed phase boundary between the B19 and the BCO began to propagate. During the movement of the phase boundary, another phase boundary formed and moved towards the first phase boundary at the opposite side speeding up the phase transformation, which was previously observed by Shaw et al. [29]. However, the stacking faults as shown in Figure 3(c) were formed gradually with the movement of the two phase boundaries due to the relative high pressure. The stacking faults developed into the deformation twins with a twinning plane of $\{1\,1\,2\}$ due to the energy release caused by the phase transformation, leading to the reverse phase transformation from the BCO to the B19, which completed until the deformation twinning-induced plastic deformation finished as illustrated in Figure 3(b) and (c). Subsequently, due to the movement of the twin boundaries as shown in Figure 3(c), the stress was released continuously during loading, leading to a vibration of stress at a nearly constant value in a strain range 5.0–10.0%.

Next, the simulation with a relative high temperature of 400 K (~50 K above the A_s and thereby the B2 phase is stable) was performed to investigate the phase transformation behaviour of the NiTi nanopillar. The stress versus strain curve and the corresponding CNA at a temperature of 400 K and at a strain rate of 8.25×10^8 s^{-1} are given in Figure 4(a), and the microstructures of the NiTi at various strains are given in Figure 4(b) and (c). As shown in Figure 4(a), the nanopillar with the initial B2 phase deformed elastically while the strain was less than 2.5%, and then the stress increased non-linearly with increasing strain, indicating the phase of the nanopillar transformed quickly to B19 in a strain increment of about 0.5%. Then, the stress increased linearly again with the increase of strain, indicating the elastic deformation of the newly formed B19 phase. The CNA values were kept at about 3.4 during the phase transformation of B2 → B19. A stress plateau was observed at a strain of about 6.1% while the formation of the B19′ phase, and the corresponding CNA increased to about 3.7. The B19′ phase transformed to the BCO phase quickly as the result of 325 K. The stress increased to the peak value of 4.5 GPa at a strain of 6.7%. Then the stress decreased sharply to 2.3 GPa at a strain of 7.4% with the movement of phase boundary between the B19 and the BCO, and the corresponding CNA continuously increased to 5.0. Similar to the result of 325 K, the second phase boundary was initiated at the opposite side speeding up the phase transformation. However, unlike the result of 325 K, the defects such as stacking faults were not initiated at the temperature of 400 K. As a result, the reverse

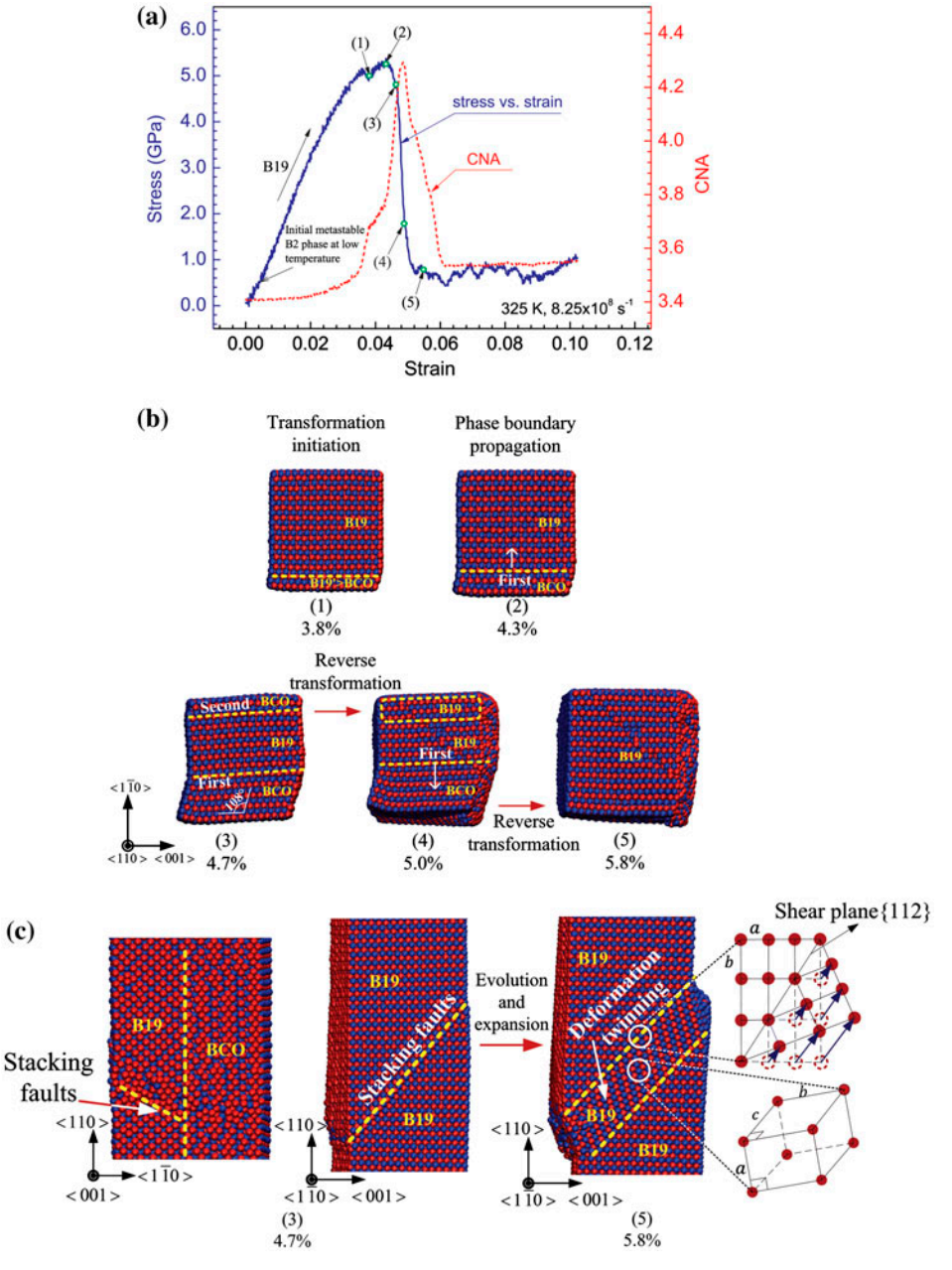

Figure 3. (colour online) Compression of NiTi nanopillar at 325 K with a constant strain rate of $8.25 \times 10^8\ s^{-1}$ up to 10.23%. (a) Stress versus strain curve of NiTi (solid line) and the average CNA values (dash line) during loading. (b) Cross-sectional view of the nanopillar at various strains, showing the phase transformation of B19 → B19′ → BCO and the reverse phase transformation of BCO → B19. (c) Lateral view of nanopillar after the plastic deformation, showing the formation of the stacking faults and the twinning deformation.

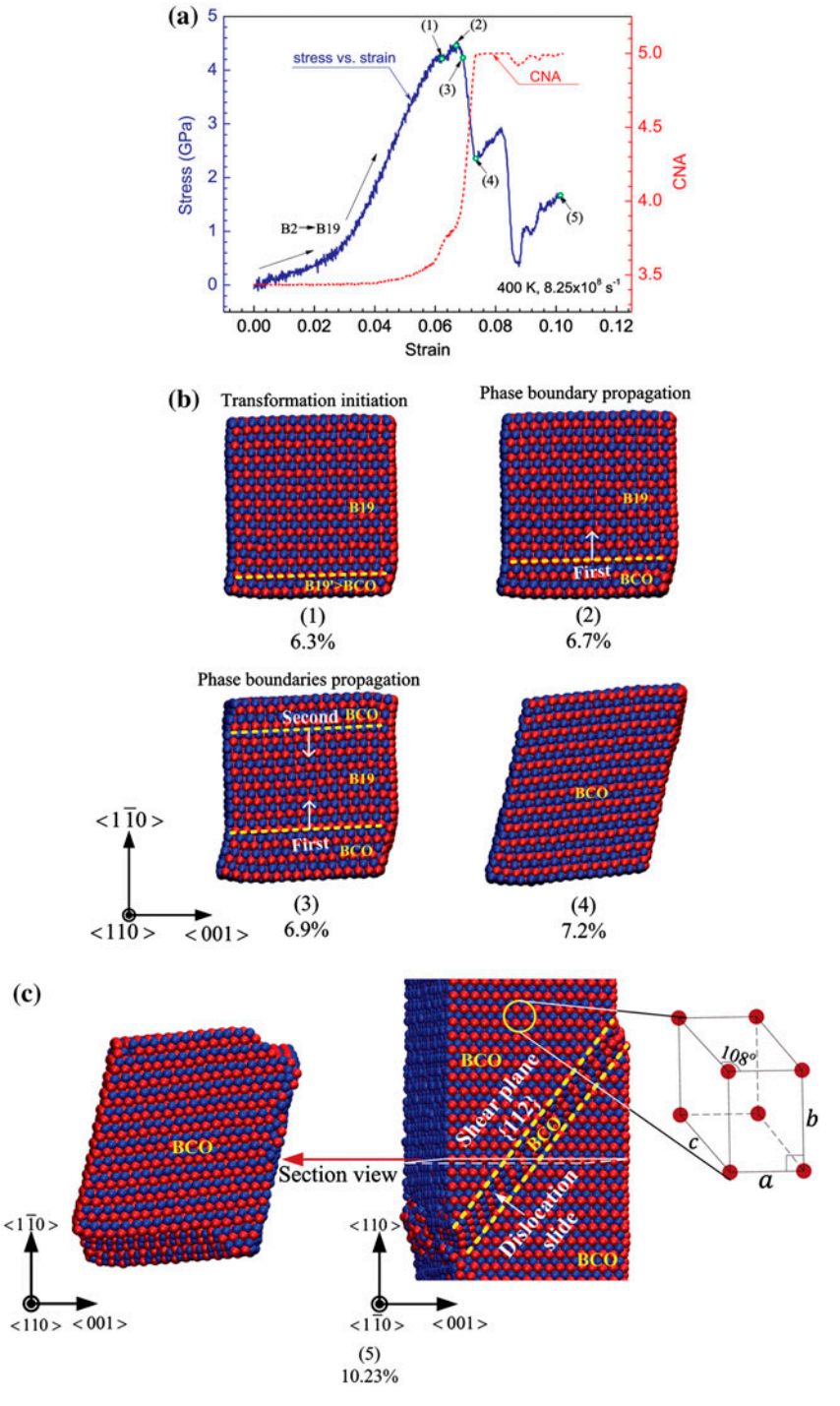

Figure 4. (colour online) Compression of the NiTi nanopillar at 400 K with a constant strain rate of 8.25×10^8 s^{-1} up to 10.23%. (a) Stress versus strain curve (solid line) and the corresponding CNA curve (dash line). (b) Cross-sectional view of the NiTi nanopillar at various strains, showing the phase transformation of B19 → B19′ → BCO. (c) Cross-sectional view and lateral view of the NiTi nanopillar after plastic deformation.

phase transformation was not observed and the B19 phase fully transformed to the BCO phase eventually. The newly formed BCO phase deformed elastically up to a strain of about 8.2%, and then the second sharp drop of stress was observed, indicating the slip-induced plastic deformation of the BCO phase as illustrated in Figure 4(c), which was shown as evident by the fluctuation of the corresponding CNA values at the strain of 8.2%.

Then, the phase transformation of the NiTi nanopillar at a high temperature of 600 K was simulated. The simulated stress versus strain curve and the corresponding CNA history are given in Figure 5(a), and the microstructure evolution during loading is given in Figure 5(b) and (c). As shown in Figure 5(a), the initial B2 phase deformed elastically until the strain increased to about 5.2%, which was much larger when compared to the results of 400 K. Note that the CNA increased a little from 3.4 to 3.6 during the elastic deformation of the initial B2 phase when compared to the result of 400 K, which could be ascribed to the increase of surface effect induced by the increase of temperature. Then, the B19 phase was formed and deformed elastically until the strain reached about 6.6 %. When the strain exceeded 6.7%, atoms shuffling on $\{1\,1\,0\}\langle 0\,0\,1\rangle$ occurred with the formation of defects as depicted in Figure 5(b). As the increase of vibration velocities of atoms at elevated temperatures, it is much easier for atoms migration during loading, leading to the formation of some defects in the NiTi nanopillar as the observation of Cao et al. [30] In addition, the stress decreased quickly from the peak value of 3.3 GPa at a strain of 7.1% to 2.1 GPa at a strain of 7.8%, and the corresponding CNA increased from 4.0 to 4.4 due to the increase of fraction of the BCO phase. It was interesting to note that when the strain exceeded 7.8%, the phase transformation from the B19 to the BCO was obstructed due to the dislocation slide initiated from the previous defects, which was consistent with the study of Nematt-Nasser et al. [8,9] and the knowledge of martensite transformation [31], and then the reverse phase transformation of BCO → B2 occurred as shown in Figure 5(b). The corresponding CNA decreased from 4.4 to 3.7 and then kept at almost the same level while the strain exceeded 8.5%, indicating the completion of the reverse phase transformation of BCO → B2 and the dislocation-induced plastic deformation of the newly formed B2 phase with further loading, respectively. Note that the slight increase of stress after the strain exceeded 8.5% should be ascribed to the interaction between the dislocation slide and the reverse phase transformation.

3.3. *Strain rate effects*

In this section, the strain rate effects on the phase transformation behaviour of the NiTi nanopillar with the initial B2 microstructure were investigated at a temperature of 400 K. Five strain rates, i.e. 3.30×10^7, 3.30×10^8, 8.25×10^8, 1.65×10^9 and $3.30 \times 10^9\ s^{-1}$ were simulated. The simulated stress versus strain curve and the corresponding CNA values at a strain rate of $3.30 \times 10^7\ s^{-1}$ are given in Figure 6. Firstly, the stress increased linearly with respect to the strain when the strain was less than 2.5%, indicating the elastic deformation of the nanopillar with the B2 phase. After that, the crystal structure experienced a continuous change of B2 → B19, leaving a non-linear increase of the stress in the strain range about 2.5 to about 3.0%. Then, the newly formed B19 phase deformed elastically until the strain exceeded about 5.5% as evident by a constant slope of the stress versus strain curve. Subsequently, three drops

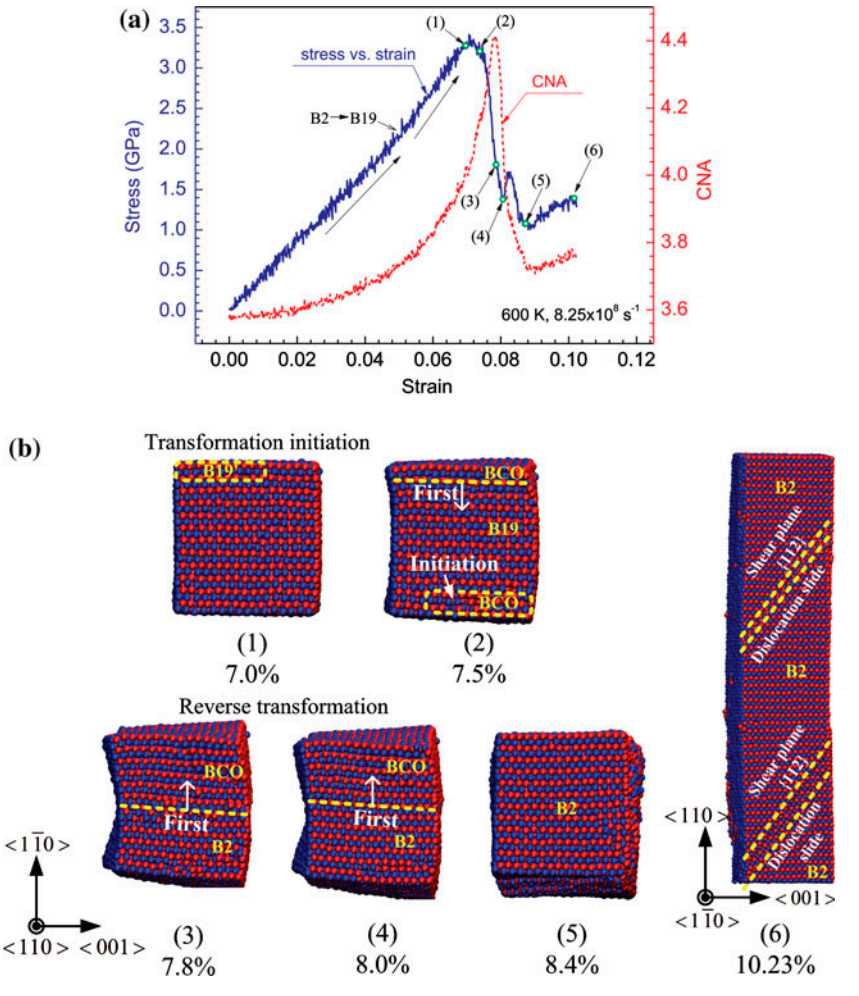

Figure 5. (colour online) Compression of the NiTi nanopillar at 600 K with a constant strain rate of 8.25×10^8 s^{-1} up to a compressive strain of 10.23%. (a) Stress versus strain curve (solid line) and the corresponding CNA (dash line). (b) Cross-sectional view of the nanopillar at various strains during the phase transformation of B19 → B19′ → BCO and the reverse phase transformation of BCO → B2. The multiple dislocations during loading were also depicted.

of stress at the strains of 5.8, 6.7 and 8.4%, respectively, were observed, indicating the initiation of the phase transformation of B19 → B19′ → BCO at the free surface of the nanopillar, the propagation of the phase transformation boundary between the B19 and the BCO and the dislocation slide-induced plastic deformation of the BCO, respectively. Beside the phase transformation of B2 → B19, the CNA values at various strains as shown in Figure 6 also clearly showed the complex phase transformation behaviour of the NiTi nanopillar. The CNA kept almost at the same level of about 3.4 before the strain reached about 5.5%. Then, the CNA increased to the first plateau with a value of about 3.7 at a strain of about 5.9% while the B19′ phase began to form and then

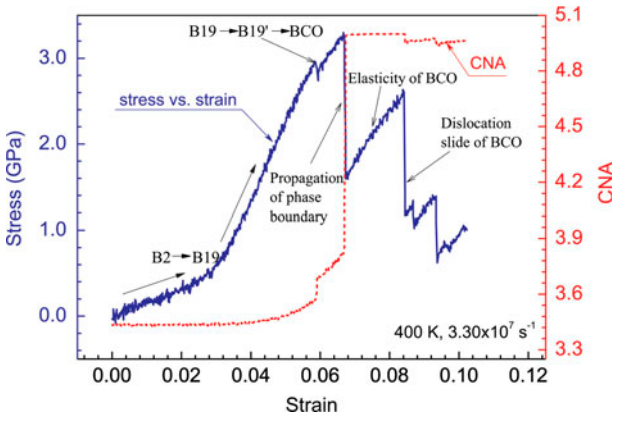

Figure 6. (colour online) Stress versus strain curve (solid line) and CNA curve (dash line) under a compressive loading rate of 3.30×10^7 s^{-1} at 400 K.

transform to the BCO phase on the lateral free surfaces. After that, the CNA increased quickly to the second plateau with a value of 5, indicating the completion of the propagation of the phase boundary between the B19 and the BCO. The abrupt drop of the CNA at a strain of about 8.4 and 9.3% was observed, indicating the dislocations slide-induced plasticity of the BCO phase.

The simulated stress versus strain curve and the corresponding CNA at a strain rate of 3.30×10^8 s^{-1} and a temperature of 400 K are given in Figure 7. It is observed that the results shown in Figure 7 shows almost the same tendency as the results at a strain rate of 3.30×10^7 s^{-1} and a temperature of 400 K. The dynamic behaviour of the nanopillar that observed at a relative low strain rate of 3.30×10^7 s^{-1} was captured at a strain rate of 3.30×10^8 s^{-1}. First, the nanopillar of parent B2 phase experienced an elastic deformation until the strain reached about 2.5% and then followed by a non-linear increase of about 0.5% indicating the phase transformation of B2 → B19. Then, the newly formed B19 phase sustained an elastic deformation until the strain reached about 5.5%. It was observed that the elastic modulus of B19 phase increased slightly when compared to the results at a lower strain rate of 3.30×10^7 s^{-1}. At the stain of about 5.9%, a slight drop of stress was observed, indicating the phase transformation of B19 → B19′ → BCO at one side of free surface. After that, a second phase boundary between the B19 and the BCO was formed and moved inside together with the afore-mentioned phase boundary, leading to an abrupt drop of stress as observed at a strain of about 6.6%. Then, the newly formed BCO phase experienced an elastic deformation until the strain reached about 8.2% and a third drop of stress was observed, indicating the dislocation slide-induced plasticity of the nanopillar with the BCO phase. The corresponding average CNA value kept at a constant value of 3.4 before the strain reached about 5.5%. Then, the CNA increased to a plateau at a strain of 6.0 with a value of 3.7 indicating the formation of first phase boundary between the B19 and the BCO. After that, the CNA increased abruptly to the second plateau with a value of 5 indicating the completion of phase transformation of B19 → B19′ → BCO. The following slight decrease of CNA was induced by the formation of dislocations slide.

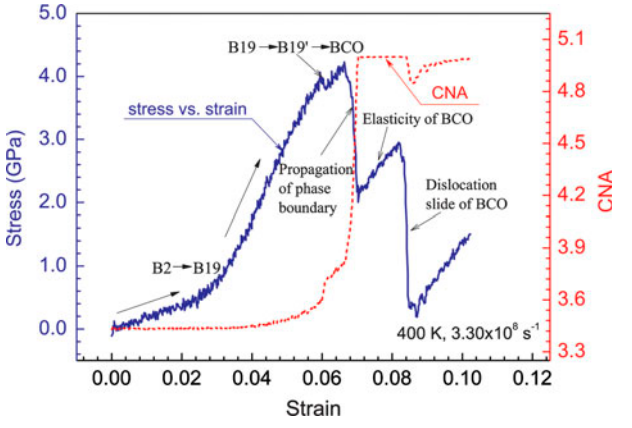

Figure 7. (colour online) Stress versus strain curve (solid line) and CNA curve (dash line) under a compressive loading rate of 3.30×10^8 s^{-1} at 400 K.

The simulated stress versus strain curve and the corresponding CNA at a strain rate of 1.65×10^9 s^{-1} and a temperature of 400 K are given in Figure 8. Similar to the result at a strain rate of 3.30×10^8 s^{-1} and a temperature of 400 K, the nanopillar experienced the phase transformation of B2 → B19 → B19′ → BCO and the dislocation slide-induced plasticity of the BCO phase. Note that the formation of the B19′ phase was represented by the stress plateau at a strain of 6.1% rather than the slight stress drop observed at the strain rate of 3.30×10^8 s^{-1} and 400 K, which could be understood by the difference of the transformation strain increments, i.e. the volume fraction increments of the newly formed BCO phase, for various strain rates in a given strain increment. Since the phase transformation speed could be supposed to be the same for a same temperature, a relative small fraction increment of the BCO phase is obtained for

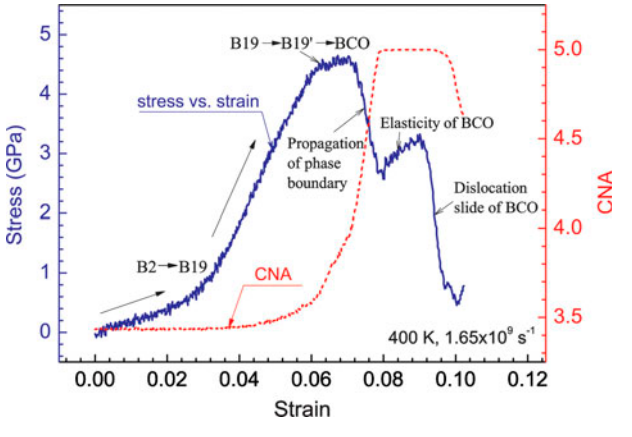

Figure 8. (colour online) Stress versus strain curve (solid line) and CNA curve (dash line) under a compressive loading rate of 1.65×10^9 s^{-1} at 400 K.

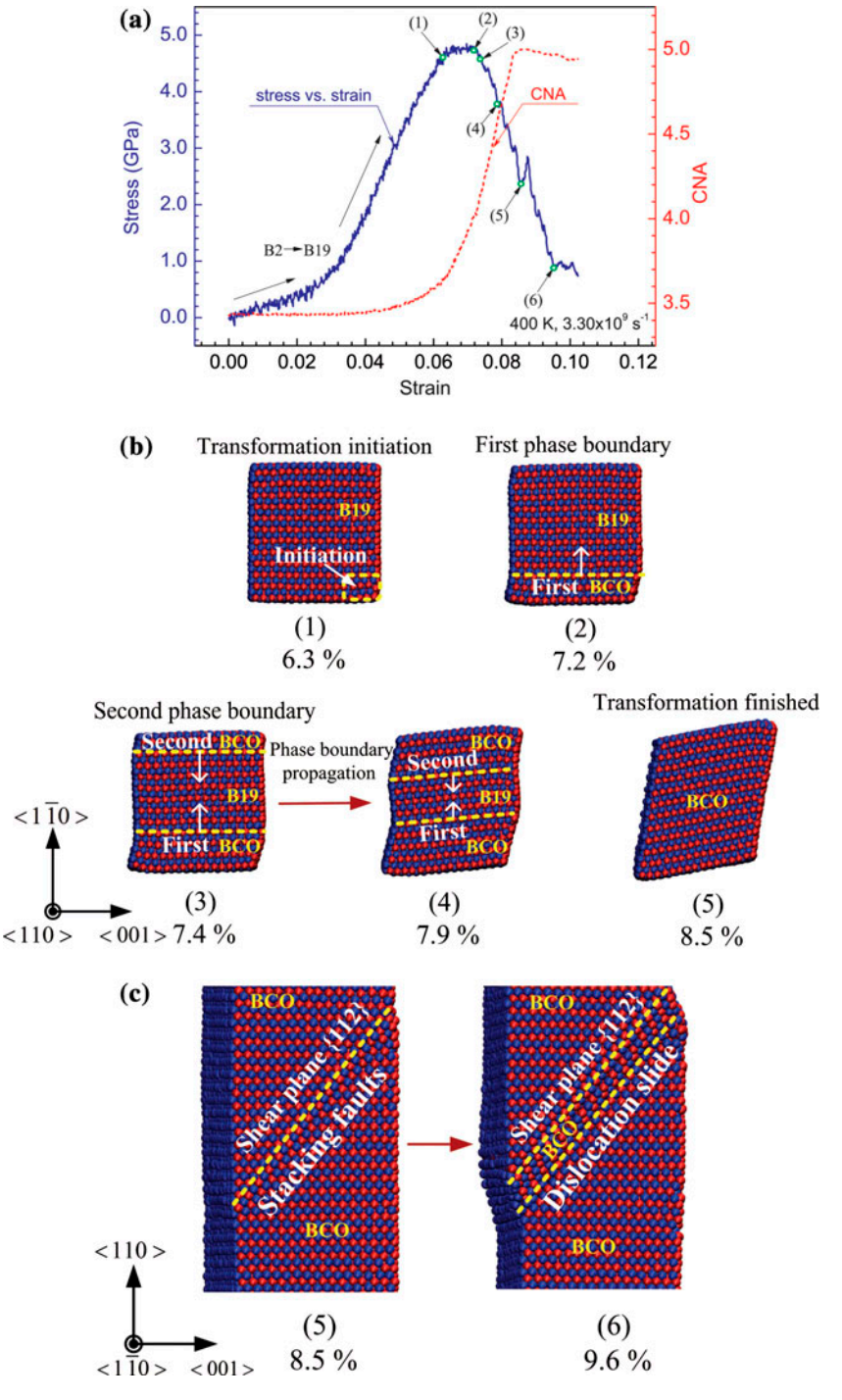

Figure 9. (colour online) (a) Stress strain curve (solid line) and CNA curve (dash line) under a compression strain rate of $3.30 \times 10^9\ s^{-1}$ at 400 K. (b) Cross-sectional view of microstructure evolution. (c) Stacking faults and dislocation slide from a lateral view.

high strain rate in the same applied strain increment, leading to the low energy release during phase transformation, and thereby the loading capacity of the nanopillar is sustained. After that, the BCO phase, which initiated on one free surface, propagated from one side to another when the strain increased to about 7.0%. During the phase propagation, another phase boundary formed at the opposite side, speeding up the phase transformation process in a strain range 7.0 to about 7.9%, leading to a large decrease of stress from 4.6 to 2.7 GPa. The newly formed BCO phase deformed elastically until the strain exceeded 9.0%. Then, an abrupt large drop of stress from 3.3 to 0.5 GPa in a strain range 9.0 to about 10.0% was observed, indicating the dislocation slide-induced plasticity of the BCO phase. The corresponding CNA value also showed the deformation behaviour of the NiTi nanopillar as depicted in Figure 8. The CNA value almost kept at a constant value of 3.4 until the strain exceeded 6.1%. Then, the CNA increased slightly to a plateau with a value of 3.8 at a strain of 6.4%, indicating the initial formation of the B19′ phase which immediately transformed to the BCO phase on the lateral free surfaces. After that, the CNA increased rapidly to the second plateau with a value of 5 at a strain of about 7.9%, indicating the completion of the propagation of the phase boundary between the B19 phase and the BCO phase. A sharp drop of CNA value was observed when the strain exceeded 9.1%, indicating the dislocation slide-induced plastic deformation of the BCO phase.

The simulated stress versus strain curve and the corresponding CNA value at a high strain rate up to 3.30×10^9 s^{-1} and a temperature of 400 K are given in Figure 9(a). As shown in Figure 9(a), the initial B2 phase deformed elastically when the strain was less than 2.5%. Then the phase transformation of B2 → B19 happened as evident by the non-linear increase of the stress in a strain range of 2.5 to about 3.0%. After that, the stress increased linearly again to the peak value of about 4.8 GPa at a strain of about 6.3%, indicating the elastic deformation of the newly formed B19 phase. Similar to the simulation results at the strain rate of 1.65×10^9 s^{-1}, the B19′ phase initiated at one free surface as shown in Figure 9(b) and immediately transformed to the BCO phase because of the surface effect. Then the stress sustained at the same level in the strain range 6.3–7.2% due to low energy release in a same strain increment for high loading rate condition. After that, a large drop of stress from 4.8 to 2.4 GPa in a strain range of 7.2–8.5% was observed, indicating the formation of second phase boundary and the propagation of phase boundaries between the B19 and the BCO as shown in Figure 9(b). Note that the stacking faults formed at the strain of 8.5 % as shown in Figure 9(c). Also, another large drop of stress from 2.8 GPa at a strain of 8.7–0.9 GPa at a strain of 9.6% was observed due to the dislocation slide-induced plasticity of the BCO phase. As shown in Figure 9(a), the corresponding CNA value also showed the complex phase transformation and the plastic deformation of the NiTi nanopillar. The CNA value kept almost at a constant value of 3.4 until the strain exceeded 6.3%. Then the CNA increased rapidly to 5 at a strain of 8.5%, indicating the completion of the phase transformation of B19 → BCO. After that, the CNA value decreased slowly from 5 to 4.9, indicating the dislocation slide-induced plasticity deformation of the BCO phase.

4. Summary of results and discussion

In the present research, the phase transformation behaviour of an NiTi nanopillar at various compressive loading rates and temperatures were simulated. It was observed

that the strain rates and the temperatures had great impact on the phase transformation behaviour of the NiTi nanopillar. The simulated stress versus strain curves and the corresponding CNA value at various temperatures and at a strain rate of $8.25 \times 10^8\ s^{-1}$ are showed in Figure 10. It could be seen that the phase transformation stress of the NiTi nanopillar and the corresponding CNA value showed high sensitivity to temperature as shown in Figure 10(a) and (b), respectively. Note that the stress for the phase transformation from the initial B2 phase to the orthorhombic B19 phase increased from about 0.15 to about 2.5 GPa with increasing temperature from 350 to 600 K. In addition, it was observed that the phase transformation stress of B19 → B19′ → BCO decreased from about 5.2 to about 3.2 GPa with increasing temperature, which could be understood by the increase of vibration velocity of atoms with increasing temperature. It was relatively easier for atoms to overcome the energy barrier for the phase transformation and reach a new equilibrium at a higher temperature, leaving to the relative

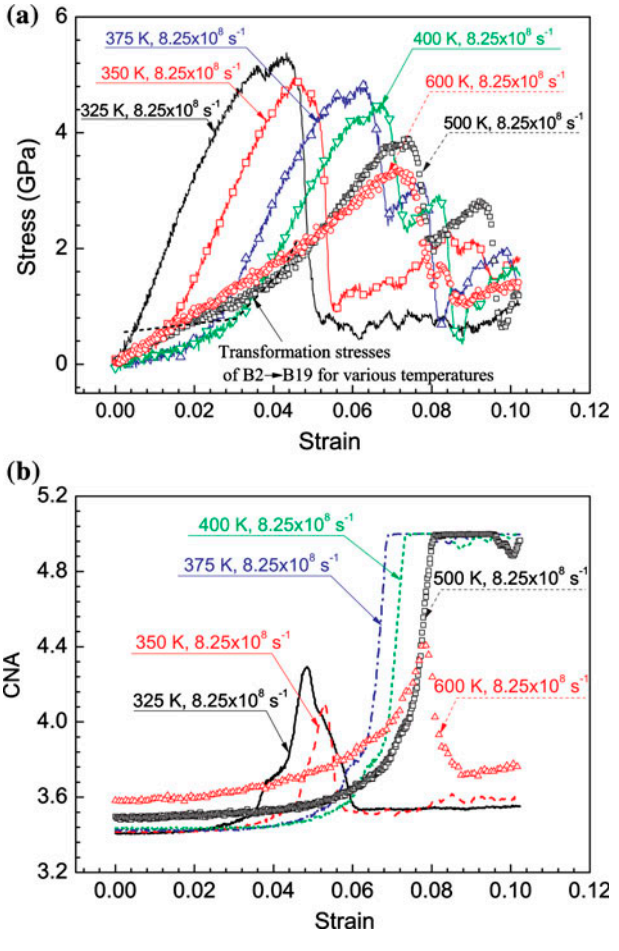

Figure 10. (colour online) (a) Stress versus strain curves and (b) corresponding CNA curves at various temperatures and at a constant compressive loading rate of $8.25 \times 10^8\ s^{-1}$.

low transformation stress from the B19 phase to the BCO phase at a higher temperature. Based on the simulation results, it could be speculated that the phase transformation of B19 → BCO would not happen at sufficient high temperature when the phase transformation stress of B19 → BCO is lower than that of B2 → B19. Moreover, the deformation twinning-induced plasticity and the dislocation slide-induced plasticity were observed during loading for various temperatures. At a low temperature of 325 K, the deformation twinning-induced plasticity, which inhibited the phase transformation, occurred during phase transformation from the B19 to the BCO. The stress was almost at a constant level with the increase of strain during the movement of the twin boundaries as shown in Figure 3(c). However, the dislocation slide-induced plasticity, which also inhibited the phase transformation, occurred at high temperatures ranging from 375 to 600 K, which could be understood by the competition mechanism between the deformation twinning and the dislocation slide at elevated temperatures. Generally, the critical twinning stress could be regarded as insensitive to strain rate and temperature, whereas the dislocation slip stress increased dramatically with increasing strain rate and with decreasing temperature [32]. Therefore, the dislocation slide-induced plasticity is the dominated plastic deformation. The stress increased after the slide band formed until another one appeared.

The corresponding CNA value as given in Figure 10(b) also clearly showed the complex phase transformation behaviour of NiTi at various temperatures. With increasing temperature, the initial average CNA value and the strain for phase transformation of B19 → B19′ increased. The peak value of CNA varied due to the different volume fraction of the formed BCO phase. At relatively low temperatures of 325 and 350 K and a high temperature of 600 K, the phase boundary between the B19 phase and the BCO phase did not propagate throughout the NiTi nanopillar due to the deformation twinning and dislocation slide-induced plasticity during phase transformation, respectively. In addition, it was observed that the value of CNA decreased almost to the same value of the initial state, indicating the reverse phase transformations of BCO → B19 at 325 and 350 K and BCO → B2 at 600 K, respectively. However, the CNA kept almost at a constant value of 5 at 375, 400 and 500 K, indicating that the reverse transformation did not happen at these temperatures. At a low temperature of 325 K, the phase transformation of B19 → BCO was demanded to accommodate the applied deformation. During this period, the energy release caused by the phase transformation drove the formation of deformation twinning, which led to further energy release, providing the driving force for the reverse transformation of BCO → B19 since it was more stable when compared to the B2 phase and the BCO phase [31]. Similarly, at a relative high temperature of 600 K, the reverse transformation of BCO → B2, which was driven by the dislocation slide deformation, occurred, since the B2 phase was more stable when compared to the B19 and the BCO phase at 600 K. However, in the other situations, e.g. at 400 K, there was no dislocation slide or deformation twin during the phase transformation of B19 → BCO, resulting in insufficient driving force for the reverse phase transformation.

The simulated stress versus strain curves and the corresponding CNA value at a temperature of 400 K and at various strain rates of 3.30×10^7, 3.30×10^8, 8.25×10^8, 1.65×10^9 and 3.30×10^9 s^{-1} are given in Figure 11(a) and (b), respectively. The stress versus strain curves as shown in Figure 11(a) and the corresponding CNA values as shown in Figure 11(b) for various strain rates were identical to each other for the strain

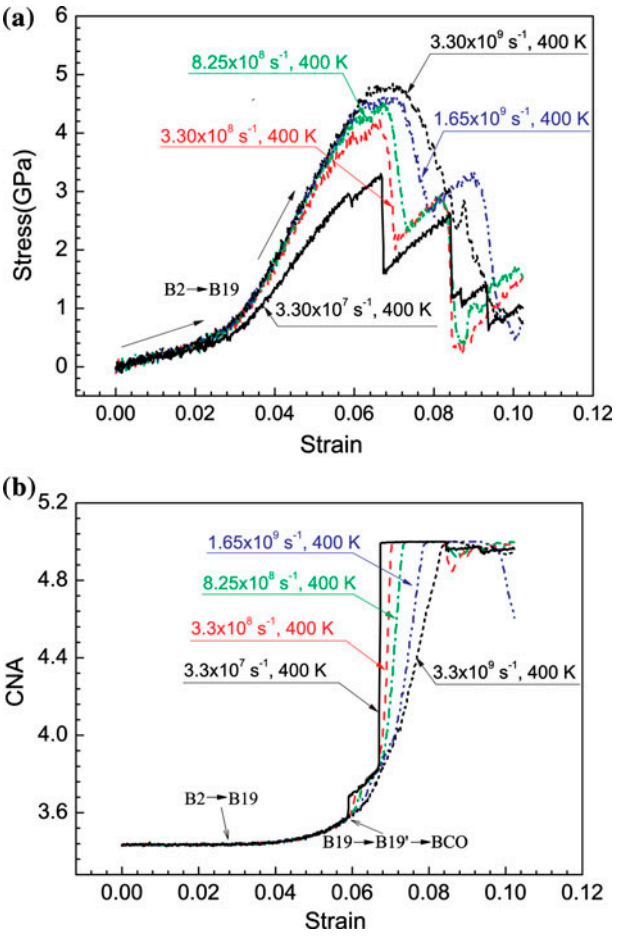

Figure 11. (colour online) (a) Stress versus strain curves and (b) corresponding CNA curves at various compressive loading rates and at a temperature of 400 K.

less than about 5.5% except a relative low elastic modulus of B19 phase at a strain rate of 3.30×10^7 s^{-1} as observed in Section 3.3, indicating the insensitivity of strain rate on the phase transformation of B2 → B19 at strain rates higher than 10^8 s^{-1}. However, the stress during the phase transformation of B19 → B19′ → BCO increased from about 3.3 to about 5 GPa and the corresponding CNA increased with different velocity for different loading rate, indicating that the change of the crystal structure of NiTi from orthorhombic to monoclinic was sensitive to the loading rate. Since the phase transformation of B19 → B19′ → BCO requires shear movement of atoms, there is not enough time for atoms to reach new equilibrium positions at a relative low temperature of 400 K which deforms at a high strain rate, leading to the increase of the phase transformation stress.

Figure 12 showed the simulated relationship between the transformation stresses of B2 → B19 and B19 → B19′ and the reciprocal of temperatures at various strain rates.

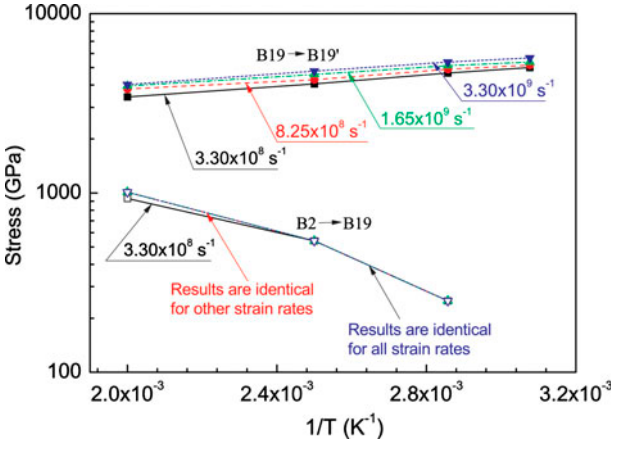

Figure 12. (colour online) Relationship between the phase transformation stresses of B2 → B19 and B19 → B19′ and the reciprocal of temperatures at various strain rates.

It was observed that at a given strain rate, the phase transformation stress of B2 → B19 increased linearly while the transformation stress of B19 → B19′ decreased with increasing temperature. In addition, at a given temperature, the transformation stresses of B2 → B19 for various strain rates were almost identical to each other, indicating that the phase transformation of B2 → B19 was insensitive to loading rate. However, the transformation stress of B19 → B19′ increased with increasing loading rate, indicating the sensitivity of loading rate on the transformation stress of B19 → B19′.

The residual crystal structures after loading at various strain rates and at various temperatures are shown in Figure 13, from which the strain rate and temperature-dependent phase diagram of NiTi is highlighted. The phase diagram was divided into regions I, II, III and IV according to the phase transformation histories. The region I

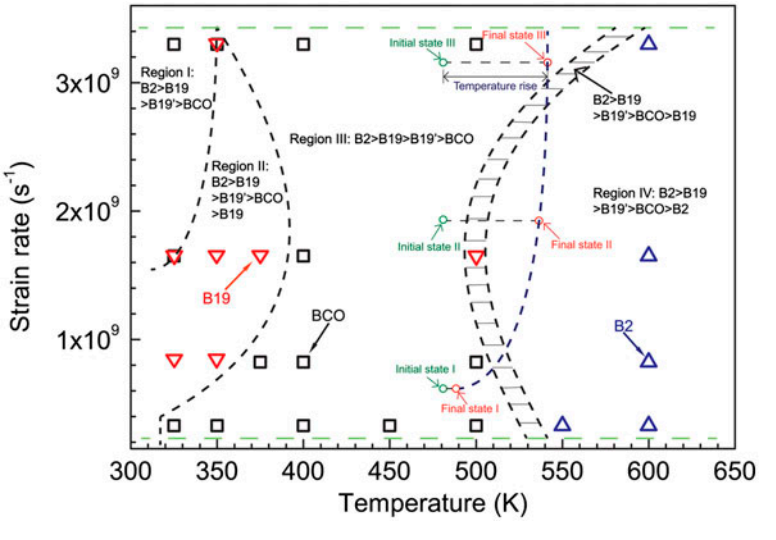

Figure 13. (colour online) Phase diagram of the NiTi nanopillar at various temperatures and at various loading rates. Different residual phases are highlighted by different shapes. Shadow region are speculated to be with the residual B19 phase.

with the serial phase transformation of B2 → B19 → B19′ → BCO and a residual BCO phase was located at temperatures lower than 350 K and strain rates higher than 1.65×10^9 s^{-1}. The reverse phase transformation would not occur in this region. The region II, which experienced the phase transformation of B2 → B19 → B19′ → BCO → B19, was located in the temperature range 325–375 K and the strain rate range 8.25×10^8–3.30×10^9 s^{-1}. Note that partial BCO phase reversely transformed to the B19 phase, i.e. the BCO phase and the B19 phase coexisted, at the boundary points between the region I and the region II, i.e. the points (325 K, 8.25×10^8 s^{-1}) and (350 K, 3.30×10^9 s^{-1}). It could be seen that the reverse phase transformation of BCO → B19 phase disappeared gradually with increasing the strain rate and decreasing the temperature at temperatures lower than 350 K. The region III, which experienced the phase transformation of B2 → B19 → B19′ → BCO, was in the temperature range 325–500 K and the strain rate range 3.30×10^8–3.30×10^9 s^{-1}. The reverse phase transformation did not occur and the BCO phase was left in this region. It is interesting to note the temperature range narrows gradually and then broadens with increasing strain rate for region III. The region IV with the phase transformation of B2 → B19 → B19′ → BCO → B2 was located at temperatures higher than 550 K and strain rates range 3.30×10^8–3.30×10^9 s^{-1}. Note that the reverse phase transformation of BCO → B2 occurred and the residual high temperature stable B2 phase was left in this region. However, the B19 phase rather than the B2 phase was left at the boundary between the region III and the region IV, i.e. the point (500 K, 1.65×10^9 s^{-1}), after the reverse phase transformation. Since the reverse phase transformation of BCO → B2 should experience the intermediate state phase of B19, the B19 phase should be left if atoms could not overcome the energy barrier between the B19 and the B2. From this point, there should be a narrow temperature region for the phase transformation of B2 → B19 → B19′ → BCO → B19 as depicted in Figure 13 by the shadow region. It is to be noted that some unrealistic high strain rates were studied in this paper when compared to experiments, which is the major issue in MD simulation. The time consumption in MD simulation will increase significantly with increasing calculation steps and the number of atoms. As a result, it will take a lot of time to investigate the phenomenon at low strain rates through MD simulation, which might be improved by high efficient computers. However, the MD simulation provides an atomic insight into the deformation behaviour of materials. The details of martensitic transformation and corresponding microstructure evolution of the NiTi nanopillar during loading at various strain rates and at various temperatures were captured. In addition, at a realistic low strain rate of 3.30×10^7 s^{-1} and at a temperature of 400 K, the NiTi nanopillar experienced the phase transformation of B2 → B19 → B19′ → BCO, which showed the same tendency of region III. More simulations will be performed at a wide temperature range and even lower strain rates in near future.

The complex phase transformation behaviour, especially the reverse phase transformation of NiTi should be ascribed to the interaction between phase transformation and plastic deformation. During the phase transformation, the energy is released, which drives the formation of deformation twinning or dislocation slide-induced plastic deformation. Further, energy release is induced during plastic deformation, providing the driving force for the reverse transformations. At relative low temperatures, the stacking faults and consequently the deformation twinning-induced plasticity occur [32], leading to the reverse phase transformation of BCO → B19 since the B19 phase is stable at low

temperatures as shown in region II. At relative high temperatures, the dislocation slide-induced plasticity occur because of the high vibration velocity of atoms [32], leading to the reverse phase transformation of BCO → B2 since the B2 phase is stable at high temperature as shown in region IV. However, at low temperatures and sufficient high strain rates, the reverse phase transformation will not occur because there is not adequate time for the reverse phase transformation as depicted in the region I. In addition, the deformation twinning or dislocation slide-induced plastic deformation does not occur when the phase transformation stress is not sufficiently high and the vibration velocities of atoms are not sufficiently fast, leading to no reverse phase transformation in the region III.

The phase transformation behaviour of NiTi obtained in the present study is helpful for understanding the controversial experimental observations of phase change of NiTi at elevated strain rates as the studies by Nemat-Nasser et al. [8,9] at various strain rates in a range of 10^{-3}–20,000 s^{-1} and at temperatures in a range of 77–400 K and Liao et al. [10] at various strain rates in a range of 10^{5}–10^{7} s^{-1} and at temperatures in a range of 273–373 K. Regard the change of crystal structure from cubic to monoclinic as nominal phase transformation observed in dynamic experiments. The residual crystal structures of NiTi after experiments are dependent on test temperatures, loading rates and applied stresses. Also, the local temperature of NiTi would change dramatically during loading [33]. Suppose there are some initial states of NiTi located in the region III as depicted in Figure 13. For the initial state I, the increase of temperature is not adequate to go across the region boundary at relatively low strain rates as in SHPB, leading to the phase transformation and the residual monoclinic phase as observed by Nasser et al. [8,9] as long as the applied stress is higher than the phase transformation stress. However, for the initial state II, there will be a considerable temperature rise for NiTi while loaded at high strain rate and at sufficient high stress. The considerable increase of temperature leads to the elimination of the phase transformation as depicted in Figure 10. Also, the yield stress of the B2 phase decreases with increasing temperature, which could lead to the plasticity of initial B2 phase prior to the phase transformation at sufficient high temperature as observed by Nasser et al. [8,9]. Nevertheless, the elimination of the phase transformation could also be ascribed to the reverse phase transformation behaviour of NiTi at high temperature as shown in Figure 13. In addition, at ultrahigh strain rate, Liao et al. [10] observed the residual transformed phase of NiTi in the laser shocked region. It might be ascribed to the reason that the temperature rise during loading is not adequate to go through the boundary between the region III and the region IV as the initial state III as depicted in Figure 13, leading to the transformed phase of NiTi after laser-induced shock. Further simulation will be conducted to investigate the dynamic response of NiTi during the propagation of shock waves to better understand its strain rate, temperature and stress-dependent phase transformation behaviour.

Acknowledgements

The authors wish to express their appreciation to Prof. T. Zhu at Georgia Institute of Technology for providing the improved potential of NiTi.

Disclosure statement

No potential conflict of interest was reported by the authors.

Funding

This work was supported by National Natural Science Foundation of China [grant number 11332011], [grant number 11402277].

References

[1] K. Otsuka and C.M. Wayman, *Shape Memory Materials*, Cambridge University Press, Cambridge, 1998.
[2] T.W. Duerig, K.N. Melton and D. Stöckel, *Engineering Aspects of Shape Memory Alloys*, Butterworth-Heinemann, London, 1990.
[3] J.W. Christian and S. Mahajan, Prog. Mater. Sci. 39 (1995) p.1.
[4] Kaushik Bhattacharya, *Microstructure of Martensite*, Oxford University Press, Oxford, 2003.
[5] K. Otsuka and X. Ren, Prog. Mater. Sci. 50 (2005) p.511.
[6] A. Biesiekierski, J. Wang, M. Abdel-Hady Gepreel and C. Wen, Acta Biomater. 8 (2012) p.1661.
[7] A. Pequegnat, M. Daly, J. Wang, Y. Zhou and M.I. Khan, Smart Mater. Struct. 21 (2012) p.094004.
[8] S. Nemat-Nasser and W. Guo, Mech. Mater. 38 (2006) p.463.
[9] S. Nemat-Nasser, J.-Y. Choi, W.-G. Guo and J.B. Isaacs, Mech. Mater. 37 (2005) p.287.
[10] Y. Liao, C. Ye, D. Lin, S. Suslov and G.J. Cheng, J. Appl. Phys. 112 (2012) p.033515.
[11] W.W. Chen, Q. Wu, J.H. Kang and N.A. Winfree, Int. J. Solids Struct. 38 (2001) p.8989.
[12] D. Gunderov, A. Lukyanov, E. Prokofiev, A. Kilmametov, V. Pushin and R. Valiev, Mater. Sci. Eng. A 503 (2009) p.75.
[13] Y. Zhong, K. Gall and T. Zhu, Acta Mater. 60 (2012) p.6301.
[14] N. Zotov, V. Marzynkevitsch and E.J. Mittemeijer, J. Alloys Compd. 616 (2014) p.385.
[15] X. Wang, Y. Bellouard and J.J. Vlassak, Acta Mater. 53 (2005) p.4955.
[16] Y. Liu, Y. Li, K.T. Ramesh and J. Van Humbeeck, Scr. Mater. 41 (1999) p.89.
[17] J. Ye, R.K. Mishra, A.R. Pelton and A.M. Minor, Acta Mater. 58 (2010) p.490.
[18] T. Simon, A. Kröger, C. Somsen, A. Dlouhy and G. Eggeler, Acta Mater. 58 (2010) p.1850.
[19] A.M. Thakur, N.N. Thadhani and R.B. Schwarz, Metall Mater. Trans. A 28 (1997) p.1445.
[20] C.D. Wu, P.H. Sung and T.H. Fang, J. Mol. Model. 19 (2013) p.1883.
[21] Y. Zhong, K. Gall and T. Zhu, J. Appl. Phys. 110 (2011) p.033532.
[22] T. Sato, K.-I. Saitoh and N. Shinke, Model. Simul. Mater. Sci. 14 (2006) p.S39.
[23] F. Daniel and J. Hannes, Comp. Mater. Sci. 2 (1994) p.279.
[24] W.S. Lai and B.X. Liu, J. Phys.: Condens. Mat. 12 (2000) p.L53.
[25] S. Plimpton, J. Comput. Phys. 117 (1995) p.1.
[26] T. Brill, S. Mittelbach, W. Assmus, M. Mullner and B. Luthi, J. Phys.: Condens. Mat. 3 (1991) p.9621.
[27] N. Hatcher, O.Y. Kontsevoi and A.J. Freeman, Phys. Rev. B: Condens. Mat. Mater. Phys. 79 (2009) p.020202.
[28] T. Ezaz, J. Wang, H. Sehitoglu and H.J. Maier, Acta Mater. 61 (2013) p.67.
[29] J.A. Shaw and S. Kyriakides, J. Mech. Phys. Solids 43 (1995) p.1243.
[30] A. Cao and E. Ma, Acta Mater. 56 (2008) p.4816.
[31] W.D. Callister and D.G. Rethwisch, *Fundamentals of Materials Science and Engineering: An Integrated Approach*, Wiley & Sons, Hoboken, NJ, 2012.
[32] C. Ye, S. Suslov, D. Lin, Y. Liao and G.J. Cheng, J. Appl. Phys. 115 (2014) p.213519.
[33] H.J. Frost and M.F. Ashby, *Deformation Mechanism Maps*, Oxford University Press, Oxford, 1982.